HHS Public Access

Author manuscript

Phys Med Biol. Author manuscript; available in PMC 2017 August 21.

Published in final edited form as:

Phys Med Biol. 2016 August 21; 61(16): 6132–6153. doi:10.1088/0031-9155/61/16/6132.

A Neural Network-based Method for Spectral Distortion Correction in Photon Counting X-ray CT

Mengheng Touch[1,2], **Darin P. Clark**[1], **William Barber**[3], and **Cristian T. Badea**[1,*]

[1]Center for In Vivo Microscopy, Department of Radiology

[2]Medical Physics Graduate Program, Duke University, Durham, NC 27710

[3]DxRay, Northridge, CA 91324

Abstract

Purpose—Spectral CT using a photon counting x-ray detector (PCXD) shows great potential for measuring material composition based on energy dependent x-ray attenuation. Spectral CT is especially suited for imaging with K-edge contrast agents to address the otherwise limited contrast in soft tissues. We have developed a micro-CT system based on a PCXD. This system enables both 4 energy bins acquisition, as well as full-spectrum mode in which the energy thresholds of the PCXD are swept to sample the full energy spectrum for each detector element and projection angle. Measurements provided by the PCXD, however, are distorted due to undesirable physical effects in the detector and can be very noisy due to photon starvation in narrow energy bins. To address spectral distortions, we propose and demonstrate a novel artificial neural network (ANN)-based spectral distortion correction mechanism, which learns to undo the distortion in spectral CT, resulting in improved material decomposition accuracy. To address noise, post-reconstruction denoising based on bilateral filtration, which jointly enforces intensity gradient sparsity between spectral samples, is used to further improve the robustness of ANN training and material decomposition accuracy.

Methods—Our ANN-based distortion correction method is calibrated using 3D-printed phantoms and a model of our spectral CT system. To enable realistic simulations and validation of our method**,** we first modeled the spectral distortions using experimental data acquired from ^{109}Cd and ^{133}Ba radioactive sources measured with our PCXD. Next, we trained an ANN to learn the relationship between the distorted spectral CT projections and the ideal, distortion-free projections in a calibration step. This required knowledge of the ground truth, distortion-free spectral CT projections, which were obtained by simulating a spectral CT scan of the digital version of a 3D-printed phantom. Once the training was completed, the trained ANN was used to perform distortion correction on any subsequent scans of the same system with the same parameters. We used joint bilateral filtration (BF) to perform noise reduction by jointly enforcing intensity gradient sparsity between the reconstructed images for each energy bin. Following reconstruction and denoising, the CT data was spectrally decomposed using the photoelectric effect, Compton scattering, and a K-edge material (i.e. iodine). The ANN-based distortion correction approach was tested using both simulations and experimental data acquired in phantoms and a mouse with our

* cristian.badea@duke.edu; phone 1 919 684-7509; http://www.civm.duhs.duke.edu/.

PCXD-based micro-CT system for 4 bins and full-spectrum acquisition modes. The iodine detectability and decomposition accuracy were assessed using the contrast-to-noise ratio and relative error in iodine concentration estimation metrics in images with and without distortion correction.

Results—In simulation, the material decomposition accuracy in the reconstructed data was vastly improved following distortion correction and denoising, with 50% and 20% reductions in material concentration measurement error in full-spectrum and 4 energy bins cases, respectively. Overall, experimental data confirms that full-spectrum mode provides superior results to 4-energy mode when the distortion corrections are applied. The material decomposition accuracy in the reconstructed data was vastly improved following distortion correction and denoising, with as much as a 41% reduction in material concentration measurement error for full-spectrum mode, while also bringing the iodine detectability to 4–6 mg/ml. Distortion correction also improved the 4 bins mode data, but to a lesser extent.

Conclusions—The results demonstrate the experimental feasibility and potential advantages of ANN-based distortion correction and joint bilateral filtration-based denoising for accurate K-edge imaging with a PCXD. Given the computational efficiency with which the ANN can be applied to projection data, the proposed scheme can be readily integrated into existing CT reconstruction pipelines.

Keywords

spectral CT; micro-CT; distortion correction; artificial neural network; material decomposition

1. INTRODUCTION

Computed tomography (CT) has been the dominant modality for imaging in both clinical and pre-clinical applications due to its very high spatial and temporal resolution. Conventional CT utilizes an energy integrating detector (EID), which measures the integrated signal produced by a polychromatic x-ray spectrum. Reconstruction yields an energy- weighted image of linear attenuation coefficients. This loss of energy information results in some major limitations to current CT technologies, including poor soft tissue contrast and reduced accuracy of mass attenuation measurements [2, 3].

To improve material discrimination, extra information on tissue composition can be provided via spectral CT by measuring the material-dependent attenuation of x-ray photons at different energies. The current clinical implementation of spectral CT, dual-energy (DE) CT, scans the same subject with two different x-ray spectra, allowing separation of two materials. We have demonstrated preclinical, functional imaging applications of EID-based DE micro-CT involving the separation of iodine and calcium or iodine and gold, including classification of atherosclerotic plaque composition [4], non-invasive measurement of lung [5] and myocardial perfusion [6], and the classification of tumor aggressiveness and therapy response in the lungs [7] and in primary sarcoma tumors [8, 9]. Several factors limit further development and adoption of DE-CT imaging protocols. Chief among these is the relative insensitivity of polychromatic x-ray spectra to energy-localized, material-specific changes in

x-ray attenuation (e.g. K-edges). This spectral insensitivity is caused by the lack of energy-resolving power associated with EIDs.

Advancements in detector technology, specifically in photon counting x-ray detectors (PCXD) [10], can mitigate the above-mentioned limitations. PCXD have already shown great promise for increasing performance in quantitative material decomposition of spectral CT data [2]. These detectors bin incoming photons based on their energy, acquiring detailed spectral information and potentially enabling the decomposition of several K-edge materials from a single scan. We have developed a micro-CT system based on a PCXD and have used it to acquire data either with the 4 hardware-based energy bins or using a larger number of bins by sweeping the energy thresholds over the full-spectrum for each detector element, so called full-spectrum mode [2, 11]. As a technique, full-spectrum CT overcomes the hardware limitations of a fixed number of energy bins and allows for post-reconstruction rebinning of detected counts, at the expense of increased dose and projection acquisition time. Thus, full-spectrum CT enables the highest spectral sampling and, potentially, the discrimination of one or more K-edge material-based imaging probes.

The spectral measurements are typically used for decomposition into physical or material basis functions, as described in [12], but show limited accuracy due to two majors issues: (i) the projection data is typically affected by spectral distortions due to physical effects in the detector such as charge sharing, K-escape energy loss, and pulse pileup [2]; and (ii) the projection data is generally very noisy due to low photon counts at high and low energies relative to the source spectrum. Consequently, the primary objectives of this work are to develop and demonstrate a novel correction for distortions and to reduce noise in photon-starved, PCXD data to improve material decomposition performance.

Various empirical methods have been proposed to compensate for PCXD spectral distortions [13, 14]. Corrections undo the distortion process, while compensation is used to offset the effect. The correction approach is ill-posed, because the number of energy bins for available PCXDs is typically between two and eight, which is much smaller than the number of parameters required to fully describe the spectrum [2]. To work well, some assumptions about the material composition are used as constraints, e.g., the object consists only of water [15, 16]. The compensation approach of PCXD degradation factors can be achieved by incorporating a PCXD model as part of the forward imaging process, and iteratively estimating either the imaged object or the line integrals using a maximum likelihood approach [17]. However, these techniques generally require a very accurate spectral distortion model of the PCXD, usually derived from monochromatic synchrotron measurements [17] or radioisotope measurements [13]. Other compensation methods to account for PCXD distortion include a lookup table approach [18] and approaches using ANN [14, 19] to estimate material composition directly from distorted spectra. These approaches do not directly correct for the spectral distortion but they act as multi-dimensional estimators to map the distorted spectrum from a set number of energy bins to a set of known material basis functions. Notably, K-edge material was not included or discussed in these previous studies. Also, although software correction techniques can be powerful in dealing with distortions, they cannot fully compensate for reduction in detector quantum efficiency (DQE) due to photon count losses caused by charge sharing effects and

characteristic x-rays, which could otherwise be addressed using hardware strategies. Some progress has been made through hardware solutions in directly addressing spectral distortion due to charge sharing between adjacent pixels. Specifically, the Medipix 3 detector uses a photon-processing chip with special circuitry to allow charge deposition in adjacent pixels to be summed and analyzed with two simultaneous energy thresholds [20, 21].

The ANN-based method we proposed here can be categorized as a correction technique, which does not require explicit knowledge of the distortion model. Due to the highly noisy nature of full-spectrum PCXD data, the ability to reduce noise is of exceptional importance for improving material detectability. In the case of K-edge material imaging [22], special attention is required when performing noise reduction in order to preserve K-edge contrast. In ref. [11], a penalized weighted least squares approach was used to reduce noise and to produce reconstruction results consistent with the expected attenuation curves of the present materials (iodine, PLA, water, and gold). Here, we use a general post-reconstruction denoising scheme for spectral CT data that can be applied regardless of material composition, spectral distortions, and differences in noise level between energy bins, making it largely system and application independent. This approach is an extension of our previously published denoising scheme based on joint bilateral filtration [1, 23].

2. METHODS

In this work, we propose combining ANN-based distortion correction and joint bilateral filtration-based denoising to mitigate both spectral distortion and noise issues in PCXD-based spectral CT. In Section 2.A, we first describe our full spectral micro-CT system and illustrate the noise and spectral distortions. To enable realistic simulations, in Section 2.B. we determine the parameters of a distortion model that match our PCXD. Next, in section 2.C. we describe the ANN-based distortion correction approach. We use 3D printing technology to create phantoms that facilitate ANN training and testing. Sections 2.D. and 2.E. are focused on describing joint bilateral filtration denoising and our material decomposition approach. The methods are tested using both simulations (Section 2.F.) and experimental spectral CT projection data acquired in phantoms containing iodine solutions and in mice (Section 2.G).

2.A. Spectral micro-CT

We have developed a micro-CT system consisting of a CdTe-based PCXD (DxRay Inc., Northridge, CA), with 4 rows of 64 detector elements, each 1.0 mm × 1.4 mm in size and 1.0-mm thick. The PCXD can be operated in 4-energy-threshold mode or energy sweeping scan mode (also known as full-spectrum mode). Full-spectrum mode densely samples the entire energy spectrum. The system uses a polychromatic x-ray tube (Varian G297) with a tungsten anode, which produces an incoming beam that is attenuated with 5.6 cm of PMMA, 0.1 cm of Al, and 0.1 cm of Cu. We used this system for acquisitions at 75kVp with 0.6mA and 1.92-second exposures at each projection angle. Each exposure was used to sample all energies. 90 projections over a 180° arc were acquired in full-spectrum mode. In full-spectrum mode, the energy threshold of the PCXD was swept in 1-keV increments, providing projection data in 24 energy bins from 27 keV to 50 keV. For an objective

comparison at the equal dose, we have used the same acquired data for full-spectrum and 4 energy bins CT reconstruction. We have synthesized the 4 energy bins projections by adding counts to 4 bins, i.e. 27–33 keV, 33–39 keV, 39–45 keV, and 45–51 keV. This corresponds to a spectral CT acquisition with energy thresholds placed at 27, 33, 39 and 45 keV. In particular, the second threshold has been selected at 33 keV to correspond to the Kedge of iodine. The other thresholds ensure sufficient counts in each bin. The source-to-detector distance is about 80 cm (mag.: ~1.1x), which allows us to use a parallel beam approximation for image reconstruction. We have imaged phantoms containing iodine solutions of different concentrations and water. The tomographic image sets were reconstructed using filtered back projection (FBP) with a Ram-Lak frequency filter for each energy bin. Two of the major limitations for spectral CT are the spectral distortions and the highly noisy nature of projections especially for acquisition with limited photon counts in each bin such as in full-spectrum CT. For 4 energy bins, noise may be less of an issue (Fig. 1).

2.B. Detector distortion modeling

One of the major limitations of PCXD-based imaging using CdTe can be the degradation of the energy response due to physical effects like charge sharing between detector elements, pulse pileup, and energy loss due to K-escape [2]. Such energy response degradation causes a distortion in the measured energy spectrum that deviates from the incoming x-ray spectrum. To fully understand and accurately simulate this distortion, a detector response function (DRF) was experimentally determined following the model first described by Schlomka et al. in [17]. The DRF model includes two Gaussian peaks: one at the incident photon's energy and one at the K-escape energy of CdTe. An additional background term models a lower-energy tail. Hence, the DRF, $R(U,E)$, at energy U resulting from incident photons of energy E interacting with the detector can be modeled as:

$$\mathrm{R(U,E)}=\mathrm{c_1(E)}\left[\frac{1}{\sqrt{2\pi}\sigma_1(\mathrm{E})}\exp\left(-\frac{(\mathrm{U}-\mathrm{E})^2}{2\sigma_1(\mathrm{E})^2}\right)+\frac{\mathrm{c_2(E)}}{\sqrt{2\pi}\sigma_2(\mathrm{E})}\exp\left(-\frac{(\mathrm{U}-\mathrm{E_e}-\mathrm{E})^2}{2\sigma_2(\mathrm{E})^2}\right)+\mathrm{B(U,E)}\right], \quad (1)$$

where σ_1 and σ_2 represent the energy spread of the incident photon peak and the K-escape peak, respectively. E_e is the average escape photon energy of the detector material (~25 keV for CdTe). The background term, $B(U,E)$, depends on both the measured and incident photon energy. $B(U,E)$ is modeled as the product of the measured energy, U, and a constant $c_3(E)$ for $U<E-3\sigma_1$ and linearly decreases to zero over the range $U=E-3\sigma_1$ to $U=E+3\sigma_1$. The constant $c_1(E)$ is a scaling factor such that the number of incoming photons in conserved. The width of the photo peak and K-escape peak are assumed to be the same (i.e. $\sigma = \sigma_1 = \sigma_2$). The constant terms $c_2(E)$, $c_3(E)$, and $\sigma(E)$ are further parameterized as follows:

$$c_2(E) = \begin{cases} a_1 exp(-a_2 E) & E > E_e \\ 0 & E < E_e \end{cases},$$
$$c_3(E) = a_3 - a_4 E,$$
$$\sigma_1(E) = \sigma_2(E) = \sigma(E) = a_5 + a_6. \quad (2)$$

The parameters in Equation 1 were derived based on the values given in [17] and based on experimental data acquired from ^{109}Cd and ^{133}Ba radioactive sources measured by our PCXD. The acquired spectra were compared with the expected spectra for these isotopes given 1-keV sampling. The sources were placed ~5 cm in front of the PCXD during sampling. A full-spectrum acquisition with an integration time of 5 seconds for each energy was performed for each of the two sources. The counts measured by each detector pixel were summed to provide a one-dimensional signal of number of counts over the energy spectrum. The spectral data was next read into MATLAB (*MathWorks Inc., Natick, MA*) and used for fitting the DRF model. The term $c_2(E)$, containing parameters a_1 and a_2, was chosen to be the same as the value given in [17]. The rest of a parameters were derived by fitting the DRF model to the measurements by selecting values that minimized the root mean square error (RMSE) of the fit. For the ^{109}Cd source spectrum, a photo peak at 22 keV was modeled. For the ^{133}Ba source, three peaks at 31 keV, 35 keV, and 81 keV were modeled and scaled by their respective branching ratios (*LBNL Isotopes Project*, http://ie.lbl.gov/toi/; *LNHB Table of Radionuclides*, http://www.nucleide.org/DDEP_WG/DDEPdata.htm).

To validate our model, a 75-kVp polychromatic x-ray spectrum produced by our Varian x-ray tube with a tungsten rotating anode and 0.7 mm of effective Al filtration was recorded in air. This recorded spectrum was compared with a degraded version of the expected spectrum. In simulations (Section 2.F), the DRF was incorporated into a forward model of the PCXD-based imaging chain in the form of a bin sensitivity function, $S_i(E)$:

$$S_i(E) = \int_{U_T^i}^{U_T^{i+1}} R_i(U, E) dU \quad i = 1, \ldots, nbin \quad (3)$$

where *nbin* is the total number of bins. $[U_T^i, U_T^{i+1}]$ is the energy threshold (T) range for the i^{th} bin.

2.C. Distortion correction based on Artificial Neural Networks

Although the PCXD provides spectral x-ray projections, the energy distortion associated with the physical system heavily diminishes the signal from K-edge materials, and hence reduces the sensitivity of K-edge material decomposition. An artificial neural network was used to reverse the distortion in the PCXD caused by the undesirable physical effects in the detector (detailed in section 2.B). The motivation for using a neural network to perform the distortion correction is to exploit its ability to learn and model the relationship between the expected and recorded spectral measurements, transforming the distorted projection data (input) to its corresponding, expected (target) projection data. The ANN-based approach we use for distortion correction is illustrated by the flowchart in Fig. 2 and contains both

training and testing. We trained the ANN to learn the relationship between the distorted spectra (i.e. each projection pixel intensity across all energies at the same angle) and the expected, distortion-free spectra in a calibration step (Fig. 2a) for both full-spectrum and 4 energy bins modes. Once the training was completed, the trained ANN can be used to perform distortion correction on any subsequent projection data acquired with the same CT system, acquisition parameters, and basis materials (Fig. 2b).

Similar to Zimmerman et al. [14], we used an ANN architecture composed of one input layer, two hidden layers, and one output layer. The input and output layers contained 24 nodes each, which correspond to 24 desired input and output energy bins (from 27 to 50 keV), respectively. Each hidden layer contains 5 neurons, each of which represents a sigmoid activation function. Each node in the output layer is modeled by a linear approximation function. In both our simulation and experimental study, the ANN was trained using the Neural Network toolbox in MATLAB. The ANN learning algorithm minimizes the mean square error between the estimated distortion corrected spectra and the true target spectra using the Levenberg-Marquardt backpropagation technique [24] implemented in MATLAB. During training, the weights of the neural network are calculated iteratively by optimizing the matching between the neural network output and the target spectrum via a minimization of the mean square errors. This requires knowledge of the ground-truth, distortion-free projections which can be obtained by simulating the scan of digital versions of 3D printed phantoms (Fig. 3) using ideal X-ray spectra for the x-ray tube and CdTe-based detector absorption generated with *Spektr* [25]. To ensure the input and target set match as closely as possible, we designed digital phantoms using Autodesk 3D modeling software. From the digital phantoms, two physical phantoms were then 3D printed using polylactic acid (PLA) plastic material and a Makerbot Replicator 2 3D printer. The phantoms were 3D printed at 0.2 mm resolution which is sufficient to ensure a negligible difference between the digital version of the phantom and its 3D printed replica, given our PCXD pixel size of 1mm × 1.4mm.

2.D. Denoising via Joint Bilateral Filtration

To address the issue of noisy full-spectrum CT data (see Fig. 1), we use joint bilateral filtration (BF) to enforce regularity within and between the reconstructed images for each energy bin [1, 23]. The objective of the denoising algorithm is summarized by the following optimization problem:

$$\mu = \arg\min_{\mu} \tfrac{1}{2}\|\mu - \mathrm{X}\|_2^2 + \lambda\Gamma(\mu). \quad (4)$$

Given the input, reconstructed spectral CT data, X, the aim is to find a denoised version of the data, μ, which best minimizes the cost specified by $\Gamma(\mu)$ for the CT data while preserving data fidelity. The data is organized in columns, with each column representing the reconstruction of a single energy bin. To compensate for the large differential in noise between energy bins, the data fidelity is weighted by one over the normalized variance of the noise measured in each bin, allowing proportionally stronger regularization for nosier energy bins. A common choice for Γ when working with piecewise constant signals is intensity

gradient sparsity: $\Gamma(\mu) = \|W\mu\|_1$, where W is a finite difference operator. Often, $\Gamma(\mu)$ is chosen to be total variation. Here, we instead use bilateral total variation (BTV), which is reduced by applying bilateral filtration (BF) [26, 27]. The algorithm solves the original cost function (Equation 4) using the split Bregman framework and the add-residual-back strategy [28, 29]. The algorithm was described in detail in [1].

2.E. Material Decomposition

One of the promises of spectral CT is improved performance in material separation via material decomposition. To decompose spectral CT data containing a mixture of different materials into quantitative, 3D maps of the concentrations of each element, we focus on a post-reconstruction decomposition method. Extending the approach of Alvarez and Macovski [12], we perform a basis material decomposition [30]:

$$\mu(\mathrm{E}) = \alpha_{\mathrm{PE}}\mu_{\mathrm{PE}}(\mathrm{E}) + \alpha_{\mathrm{CS}}\mu_{\mathrm{CS}}(\mathrm{E}) + \alpha_{\mathrm{I}}\mu_{\mathrm{I}}(\mathrm{E}). \quad (5)$$

For our implementation, the first two terms in Equation (5) describe the energy-dependent attenuation, $\mu(E)$, in terms of the photoelectric effect (PE) and Compton scattering (CS). These PE and CS components are scaled to sum to the attenuation of water when $\alpha_{\mathrm{PE}} = \alpha_{\mathrm{CS}} = 1$. The 3rd term is the attenuation of the K-edge material, iodine (Fig. 4). The material decomposition is performed with the system calibrated material sensitivity matrix M consisting of μ_{PE},μ_{CS} and μ_{I}. Our post-reconstruction material decomposition enforces a non-negativity constraint on the material concentrations, C.

$$\mathrm{C} = \arg\min_{\mathrm{C}} \tfrac{1}{2}\|\mu - \mathrm{MC}\|_2^2 \text{ subject to } \mathrm{C} \geq 0. \quad (6)$$

The optimization in Equation (6) reflects the physical reality that concentrations cannot be negative and is enforced by subspace projection of the least squares material decomposition. In general, negative concentrations in contrast enhanced regions result from noise and distortion present in the source data.

2.F. Simulations

We performed a realistic simulation using Spektr [25] to generate ideal projection spectra of a phantom containing vials with 0 to 14 mg/ml of iodine in water, the typical concentrations that we encounter using an iodinated blood pool contrast agent in mouse studies [31]. The distortion, derived for our system using the spectral model (see Section 2.B.), was introduced into the ideal sinograms to simulate a set of spectrally distorted projections as closely matched to our PCXD measurements as possible. Poisson noise was added to match the level of noise and the number of photon counts in the real sinograms for each energy bin. The distorted and ideal spectral projections were then fed into our ANN training as input and target, respectively to provide training. The training was done using 180 projections of a simulated tomographic calibration scan (90 raw, noisy projections and 90 re-projections of BF filtered reconstructions). The mixed use of noisy and denoised projections was preferred

for training such that ANN could learn some denoising capabilities. Once the ANN training was completed, a different test phantom containing square vials with 0 to 14 mg/ml of iodine in water was simulated in a similar manner (see Fig. 3). The trained ANN was then applied to the distorted projections of the test phantom to obtain distortion corrected projections. Spectrally corrected images were then reconstructed from the corrected projections for both full-spectrum and 4 energy bins using FBP and denoising with joint BF. We performed basis material decomposition into CS, PE, and I maps. Additionally, we computed the contrast-to-noise ratio (CNR):

$$\mathrm{CNR}=\frac{|\mathrm{m}_1-\mathrm{m}_2|}{\sqrt{\sigma_1^2+\sigma_2^2}}$$

where m refers to mean values and σ to standard deviations computed in two regions of interest. In the resulting images CNR was computed for the iodine relative to water. CNR was used to estimate the iodine detectability levels (Rose's criterion: CNR ≥5 [32]) and percent relative errors for iodine concentration were evaluated and compared with and without distortion correction.

2.G. Experimental data

Similar to the simulation study, our experiments were performed in two steps: (a) a training/calibration step using the training phantom and (b) the application of the ANN on a test phantom, as shown in the flow chart in Fig. 2. The ANN training processes for the full-spectrum and 4 energy bins cases, used sets of raw, distorted projections acquired with our PCXD and corresponding sets of ideal projections without distortion obtained using the 3D digital phantom as a training target. As input to our ANN training, a set of 90 distorted projections over 180 degrees were acquired by scanning our physical phantom with vials containing water and 1, 3, 5, 7, 9, or 11 mg/ml of iodine solution (Fig. 3). From the acquired projections, we reconstructed images using FBP at each energy and averaged them to form a less noisy energy averaged image. We then performed an image registration between the digital phantom and the energy averaged image using MATLAB's phase correlation-based image registration algorithm. The corresponding target set for the training was synthesized from the registered digital phantom using the ideal x-ray spectrum and material attenuation generated by *Spektr* and the NIST XCOM database [33]. The training set was appended with another set of 90 distorted projections reprojected from the denoised version of the raw images using joint BF and was matched to the same target to provide a less noisy estimate of the input data. After the ANN was trained, it was applied to a different test phantom fabricated with the same material but with different geometry (Fig. 3).

To further illustrate the use of the ANN distortion correction, a C57BL/6 mouse was scanned using our custom PCXD-based micro-CT system. The mouse was injected via tail vein with 0.3 ml of a liposomal iodinated contrast agent [31]. Next, the animal was euthanized and scanned using full-spectrum acquisition at the same parameters as in the experimental phantoms. The full-spectrum and the 4 energy bins projections of the mouse were then fed into the corresponding ANN trained using the phantom described above to

perform spectral distortion correction. The distortion corrected projections were then reconstructed using FBP and denoised via joint BF. Material decomposition was performed using both the full-spectrum and 4 energy bins data in the same manner detailed in Section 2.E. using a material sensitivity matrix measured from the training/calibration phantom data for the corresponding with and without distortion correction cases.

To provide better anatomical reference for comparison, the same mouse was scanned at higher resolution using another PCXD detector (Pilatus 300K CdTe detector from DECTRIS; *Baden, Switzerland*) with a single threshold set at 20keV. This detector has a pixel size of 172 μm × 172 μm. We note that we used this PCXD only to provide an image for anatomical reference and that its spectral capabilities were not relevant for this study. The x-ray source for this high resolution scan was a Thermo Scientific™ PXS10 MicroFocus x-ray tube used at 80kVp, 251μA and with an integration time of 10ms per exposure.

3. RESULTS

3.A. PCXD Spectral Distortion Modeling

The results of spectral distortion modeling are presented in Fig. 5 and Table 1. Figs. 5A and B compare the model fitted and experimentally measured spectra for ^{109}Cd and ^{133}Ba, respectively. The measured spectral peaks appear to be accurately positioned using our CdTe-based PCXD. The full width at half maximum (FWHM) for the most significant peaks were 2.9 keV for ^{109}Cd (at 22 keV) and 3.2 keV for ^{133}Ba (at 31 keV). Fig. 5C shows the undistorted, 75 kVp, polychromatic tungsten spectrum (0.7 mm Al filtration, provided by Spektr [25]) and the corresponding modeled distorted x-ray spectrum along with the measured x-ray spectrum in air (no object between the x-ray source and the detector) using our PCXD. The distortion model applied to the simulated 75-kVp x-ray spectrum closely matched the measured spectrum. For a quantitative comparison, we also computed the root mean square error (RMSE) between the measured and modeled spectra from 10 to 75 keV to quantify the accuracy of the model. The resulting RMSE values for the normalized spectra were 0.0111, 0.0069 and 0.0016, respectively, for ^{109}Cd, ^{133}Ba, and the 75 kVp polychromatic spectrum. Finally, Fig. 5D displays the DRF as a matrix in which we note the low-energy tailing effect and the K escape peak from CdTe for incident photons with an energy higher than 25 keV.

3.B. Simulation Results

Our simulation results show that the distortion correction with an ANN performed notably well in correcting the distortion in our test phantom and effectively recovered the K-edge of iodine at ~34 keV (Fig. 6) in both full-spectrum and 4 energy bins case. Due to lack of space, we only show the full-spectrum CT images between 31 and 35 keV, which includes the iodine K-edge for the full-spectrum CT. Joint BF was applied to the images before decomposition to further reduce noise. It is evident that without distortion correction the spectral decomposition provides inaccurate results with tremendous iodine contamination in the CS image (Fig. 7). Once distortion correction was applied, the material decomposition was greatly improved. All vials containing iodine were clearly separated from water and the PLA container, and the mean relative error in measured iodine concentration was reduced by

50% for full-spectrum mode and 20% for 4 bins mode compared with the uncorrected result (Table 2). The detectability (Rose's criterion CNR ≥5) computed in the iodine map was also improved in the full-spectrum mode to <2mg/ml with distortion correction from more than 4mg/ml without distortion correction.

3.C. Experimental results

Fig. 8 illustrates the efficacy of the joint BF operation in removing noise from heavily photon-starved CT data acquired with our PCXD in full-spectrum mode. It is evident that the very high noise level severely limits the utility of the raw full-spectrum images. After performing joint bilateral filtration on all the spectral images (in the energy range of interest from 27 to 50 keV), the reconstructed image noise (standard deviation in water vial) is reduced by up to 98% relative to the original noise level in the raw images. Upon inspection, there is no visible structure in the residual image, which indicates that the filtration operation performed well in removing only noise while preserving the edges and structures from the raw images. In 4 bins mode, the improvement is less striking but result in up to an 86% reduction in image noise.

The experimental results further validated the ability of the ANN to perform distortion correction after training with 180 projections (90 raw noisy projections and 90 re-projections of BF filtered images) of a tomographic calibration scan. The test phantom results are shown in Fig. 9. The iodine K-edge recovery at ~34 keV and noise reduction can be noted in the distortion corrected and denoised results. As shown in both Figs. 9 and 10, the iodine K-edge was smeared out along the energy dimension in images reconstructed from spectrally distorted projections, but it was clearly recovered by distortion correction at the correct energy around the K-edge (i.e. ~34 keV). The ANN distortion correction also provides some denoising. In full-spectrum mode where noise issue is very severe, the noise was reduced by up to 86% following ANN distortion correction. Fig. 10 presents the line attenuation plots measured for a vial containing 8 mg/ml of iodine concentration, and a water vial with and without distortion corrections. While the distortion correction brings back the K-edge of iodine, some bias for water are also noted especially in the full-spectrum mode.

As Fig. 11 shows, the performance of material decomposition was serverely limited by the spectral distortion, resulting in misclassification of iodine into PE and CS and in underestimation of the iodine concentrations. Consistent with our simulation results, the improvement in material decomposition with our ANN distortion correction is evident. In full-spectrum mode, the mean relative error in iodine concentration estimation was reduced to 10% with the distortion correction from 51% without correction, a 41% improvement in material decomposition accuracy. In 4 bins mode, as shown in Fig. 11, the material decomposition could not yield meaningful results without the distortion correction. However, the corrected material decomposition improves, but shows a 33% mean relative error in iodine concentration estimation (Table 3). In the full-spectrum mode, the iodine detectability was improved from 8–10 mg/ml to 6–8 mg/ml following distortion correction. In 4 bins mode, although the mean iodine concentration estimation is not as accurate, the detectability is at 4–6 mg/ml. These results are confirmed by Fig. 12 where we plot the mean concentrations and standard deviations for each iodine vials.

Finally, Figs. 13 and 14 show our murine experimental results. A high-resolution scan is shown in Fig. 13(c) to provide anatomical reference to the lower resolution spectral CT scan. An axial slice across the heart of the mouse was reconstructed in both full-spectrum and 4 bins mode. The reconstructed images were denoised using our joint BF, providing high fidelity images even in the extremely photon-starved energy bins in the full-spectrum case. The iodine in the blood pool can be clearly seen as enhancement in the heart. However, the K-edge contrast was smeared out along the energy dimension if the distortion is left uncorrected. A comparison between the spectral distortion corrected and uncorrected images validates the iodine K-edge recovery with distortion correction at ~34keV. Fig. 14 highlights the material decomposition improvement with our ANN-based spectral distortion correction. Corrected full-spectrum CT provides superior results compared to 4 bins mode. With ANN distortion correction, the CS and PE physical basis images are relatively homogeneous throughout the mouse body, with attenuation values near the expected values for water. Without distortion correction in the 4 bins case, the CS component was heavily underestimated, causing overestimations in the PE and iodine basis images.

4. DISCUSSION AND CONCLUSIONS

The objectives of this work were to develop and demonstrate a novel ANN-based technique to correct for distortion in PCXD-based spectral CT data to improve material decomposition performance. Both full-spectrum and 4 energy bins modes were investigated. The proposed technique trained a neural network to learn the non-linear relationship between the distorted spectra recorded by the PCXD and their corresponding ideal, distortion-free spectra without requiring a specific model of the detector distortion. Using 3D modeling and 3D printing technology, the ANN training was performed as a calibration step after which the trained ANN can be used to correct for distortion in any subsequent scans on the same system and the same scanning parameters (kVp, mAs) and basis materials. This correction scheme puts most of the computational stress on the calibration (training) process, while the distortion correction operation itself requires negligible computation. Thus, our method allows seamless integration into any existing imaging frameworks without imposing additional constraints. Since our ANN-based distortion correction is done on projection data, the resulting distortion corrected projections can be used with any reconstruction and material decomposition algorithms. Given that our technique does not require accurate knowledge of the spectral distortion model, the strenuous synchrotron measurements and calibration required with other techniques such as in [17] can be eliminated. Additionally, the joint bilateral filtration denoising algorithm further augmented our ability to deal with extremely noisy spectral CT data at dense energy sampling as in full-spectrum CT.

The results demonstrate the feasibility of using an ANN to correct for spectral distortion in spectral CT imaging. In both full-spectrum and 4 energy bins mode, the accuracy in estimating the iodine concentration was improved; however only full-spectrum mode lead to better detectability after correction due to both better contrast achieved by denser energy sampling and adequate noise reduction enabled by joint bilateral filtration. In general, the inherently lower noise level in the 4 bins mode leads to better detectability. However, even with distortion correction the accuracy in estimating iodine concentration using 4 energy bin data is still lower than using the full-spectrum data.

The experiments validate the technique and applicability of the ANN trained on a 3D printed phantom to undo the distortion in another phantom with distinctly different geometry and in a mouse. Overall, the experimental data confirms that full-spectrum mode provides superior results to 4-energy mode when the distortion corrections is applied.

The limitations of our technique include some bias added by the distortion correction (see Fig. 10), causing the water attenuation spectrum to show a discontinuity at 34 keV and making it appear to contain a K-edge material (i.e. iodine). This could lead to inaccuracy in material concentration measurements. However, the magnitude of this bias (less ~ 2 mg/ml equivalent of iodine) is below the level of iodine concentration we could detect, making its contribution to iodine misclassification a rather small background in the iodine image. As a software correction method, our technique is also limited in that it cannot recover the photons lost in charge sharing events, which could only be addressed by acquisition hardware design modification [20, 21].

Although we have focused here only on iodine (the most commonly used material in CT contrast agents), in theory, the same technique could be used to image multiple K-edge materials by extending the training data set to include all the Kedge materials either by addition of the new materials in the same training phantom or by appending additional phantom scans containing the new materials. However, with multiple probes other limitations may arise including the proximity between their K-edges, position of the K-edges relative to source spectrum, and the very large variation of photon flux in different energy bins depending on the source spectrum making it a great challenge to choose a source spectrum that is optimized for multiple K-edge materials. We plan to explore the limits of our ANN-based distortion corrections with multiple contrast agents in future work.

This work explored and demonstrated the feasibility of full-spectrum CT with 1 keV energy sampling that has rarely been attempted before. However for such a case, photon starvation becomes a challenge. Our success in applying ANN-based distortion correction greatly benefited from joint BF-based denoising. We have also applied our distortion correction to the more practical case of 4 energy bins that has the benefit of lower noise level but at the cost of lower energy resolution, which limits the accuracy of the material decomposition. It is also worth noting that the 4-bin data used in our studies were synthesized from the full-spectrum scan to provide a more direct comparison at equal dose. However, the 4-bin mode implemented in most photon counting detectors uses a discriminator circuit in the hardware [10], which would provide data with different noise correlation properties relative to our study [34, 35]. Further work can be done to improve on our technique, including optimization of the ANN architecture, number of energy bins, the chosen energy thresholds and the selection and amount of training data to control the bias in correcting for distortion in non K-edge materials. Future direction also includes finding the optimal number of energy bins to balance the trade-off between radiation dose, bias, and variance in the material decomposition, which are influenced by both image noise and contrast. In this study, we controlled the issue of pulse pile-up by limiting the tube voltage and photon flux using attenuators. In future work, we also plan to test our method in the presence of pulse pile-up with higher fluxes and broader spectra at higher kVp.

In conclusion, we have outlined and demonstrated a complete framework for full-spectrum CT combining ANN-based distortion correction and denoising with joint BF, which led to improved material decomposition accuracy in K-edge imaging of iodine. By combining the two tools, we were able to address two main challenges facing PCXD-based spectral CT and to apply the framework to improve quantitative material decomposition accuracy. Given the computational efficiency with which the ANN can be applied to projection data, the proposed scheme will readily integrate into existing CT reconstruction pipelines.

Acknowledgments

All work was performed at the Duke Center for In Vivo Microscopy, an NIH/NIBIB national Biomedical Technology Resource Center (P41 EB015897), with additional funding from the National Cancer Institute (R01 CA196667). The authors acknowledge Devin Miles and the Duke Innovation Studio for assistance with 3D printing the phantoms. We thank George Tudosie from DECTRIS (Baden, Switzerland) for the loan of Pilatus 300K CdTe detector. We also thank Dr. Terry Yoshizumi and the Duke University Radiation Safety Division for access to the radioisotope sources used to calibrate our spectral distortion model.

References

1. Clark DP, et al. Simultaneous imaging of multiple contrast agents using full-spectrum micro-CT. Medical Imaging 2015: Physics of Medical Imaging. 2015:9412.
2. Taguchi K, Iwanczyk JS. Vision 20/20: Single photon counting x-ray detectors in medical imaging. Med Phys. 2013; 40(10):100901. [PubMed: 24089889]
3. Ballabriga R, et al. Review of hybrid pixel detector readout ASICs for spectroscopic X-ray imaging. Journal of Instrumentation. 2016:11.
4. Bhavane R, et al. Dual-energy computed tomography imaging of atherosclerotic plaques in a mouse model using a liposomal-iodine nanoparticle contrast agent. Circ Cardiovasc Imaging. 2013; 6(2): 285–94. [PubMed: 23349231]
5. Badea CT, et al. Dual-energy micro-CT of the rodent lung. American Journal of Physiology-Lung Cellular and Molecular Physiology. 2012; 302(10):L1088–L1097. [PubMed: 22427526]
6. Ashton JR, et al. Anatomical and functional imaging of myocardial infarction in mice using micro-CT and eXIA 160 contrast agent. Contrast Media Mol Imaging. 2014; 9(2):161–8. [PubMed: 24523061]
7. Ashton JR, et al. Dual-Energy Micro-CT Functional Imaging of Primary Lung Cancer in Mice Using Gold and Iodine Nanoparticle Contrast Agents: A Validation Study. PLoS One. 2014; 9(2):e88129. [PubMed: 24520351]
8. Clark DP, et al. In vivo characterization of tumor vasculature using iodine and gold nanoparticles and dual energy micro-CT. Physics in Medicine and Biology. 2013; 58(6):1683. [PubMed: 23422321]
9. Moding EJ, et al. Dual-energy micro-computed tomography imaging of radiation-induced vascular changes in primary mouse sarcomas. International Journal of Radiation Oncology, Biology, Physics. 2013; 85(5):1353–1359.
10. Iwanczyk JS, et al. Photon Counting Energy Dispersive Detector Arrays for X-ray Imaging. IEEE Trans Nucl Sci. 2009; 56(3):535–542. [PubMed: 19920884]
11. Gonzales B, Lalush D. Full-spectrum CT reconstruction using a weighted least squares algorithm with an energy-axis penalty. IEEE Trans Med Imaging. 2011; 30(2):173–83. [PubMed: 20409988]
12. Alvarez RE, Macovski A. Energy-selective reconstructions in X-ray computerized tomography. Phys Med Biol. 1976; 21(5):733–44. [PubMed: 967922]
13. Cammin J, et al. A cascaded model of spectral distortions due to spectral response effects and pulse pileup effects in a photon-counting x-ray detector for CT. Med Phys. 2014; 41(4):041905. [PubMed: 24694136]
14. Zimmerman KC, Schmidt TG. Experimental comparison of empirical material decomposition methods for spectral CT. Phys Med Biol. 2015; 60(8):3175–91. [PubMed: 25813054]

15. Kappler S, et al. Quantum-counting CT in the regime of countrate paralysis: introduction of the pile-up trigger method. 2011:610T.
16. Kraft E, et al. Experimental evaluation of the pile-up trigger method in a revised quantum-counting CT detector. 2012
17. Schlomka JP, et al. Experimental feasibility of multi-energy photon-counting K-edge imaging in pre-clinical computed tomography. Phys Med Biol. 2008; 53(15):4031–47. [PubMed: 18612175]
18. Alvarez RE. Estimator for photon counting energy selective x-ray imaging with multibin pulse height analysis. Med Phys. 2011; 38(5):2324–34. [PubMed: 21776766]
19. Woo-Jin, L., et al. Material depth reconstruction method of multi-energy X-ray images using neural network; Engineering in Medicine and Biology Society (EMBC), 2012 Annual International Conference of the IEEE; 2012.
20. Ballabriga R, et al. The Medipix3RX: a high resolution, zero dead-time pixel detector readout chip allowing spectroscopic imaging. Journal of Instrumentation. 2013:8.
21. Koenig T, et al. How spectroscopic x-ray imaging benefits from inter-pixel communication. Physics in Medicine and Biology. 2014; 59(20):6195–6213. [PubMed: 25255737]
22. Ghadiri H, et al. K-edge ratio method for identification of multiple nanoparticulate contrast agents by spectral CT imaging. Br J Radiol. 2013; 86(1029):20130308. [PubMed: 23934964]
23. Clark DP, Badea CT. Spectral diffusion: an algorithm for robust material decomposition of spectral CT data. Phys Med Biol. 2014; 59(21):6445–66. [PubMed: 25296173]
24. Hagan MT, Menhaj MB. Training Feedforward Networks with the Marquardt Algorithm. Ieee Transactions on Neural Networks. 1994; 5(6):989–993. [PubMed: 18267874]
25. Siewerdsen JH, et al. Spektr: a computational tool for x-ray spectral analysis and imaging system optimization. Med Phys. 2004; 31(11):3057–67. [PubMed: 15587659]
26. Elad M. On the origin of the bilateral filter and ways to improve it. IEEE Trans Image Process. 2002; 11(10):1141–51. [PubMed: 18249686]
27. Farsiu S, et al. Fast and robust multiframe super resolution. IEEE Transactions on Image Processing. 2004; 13(10):1327–1344. [PubMed: 15462143]
28. Osher S, et al. An iterative regularization method for total variation-based image restoration. Multiscale Modeling & Simulation. 2005; 4(2):460–489.
29. Gao H, et al. Multi-energy CT based on a prior rank, intensity and sparsity model (PRISM). Inverse Probl. 2011; 27(11)
30. Roessl E, et al. Sensitivity of photon-counting based K-edge imaging in X-ray computed tomography. IEEE Trans Med Imaging. 2011; 30(9):1678–90. [PubMed: 21507770]
31. Mukundan S Jr, et al. A liposomal nanoscale contrast agent for preclinical CT in mice. AJR Am J Roentgenol. 2006; 186(2):300–7. [PubMed: 16423931]
32. Rose A. The sensitivity performance of the human eye on an absolute scale. J Opt Soc Am. 1948; 38:196–208. [PubMed: 18901781]
33. Berger, MJ.; Hubbell, JH.; Seltzer, SM.; Chang, J.; Coursey, JS.; Sukumar, R.; Zucker, DS.; Olsen, K. XCOM: Photon Cross Section Database. National Institute of Standards and Technology; Gaithersburg, MD: 2010.
34. Roessl E, Ziegler A, Proksa R. On the influence of noise correlations in measurement data on basis image noise in dual-energylike x-ray imaging. Med Phys. 2007; 34(3):959–66. [PubMed: 17441242]
35. Schmidt TG, Zimmerman KC, Sidky EY. The effects of extending the spectral information acquired by a photon-counting detector for spectral CT. Phys Med Biol. 2015; 60(4):1583–600. [PubMed: 25615511]

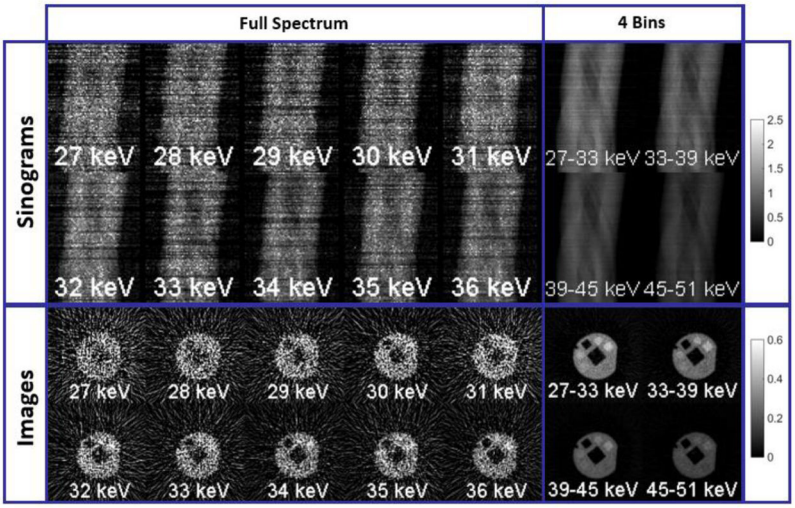

Fig. 1.

Spectral CT data acquired for a physical 3D-printed phantom in full-spectrum and 4 bins mode using the same photon flux. (Top) System-calibrated and log-transformed sinograms. (Bottom) FBP reconstructions of the sinogram data. Note the noise in the sinograms and reconstructions in full-spectrum mode. The units of the calibration bars are in cm^{-1}.

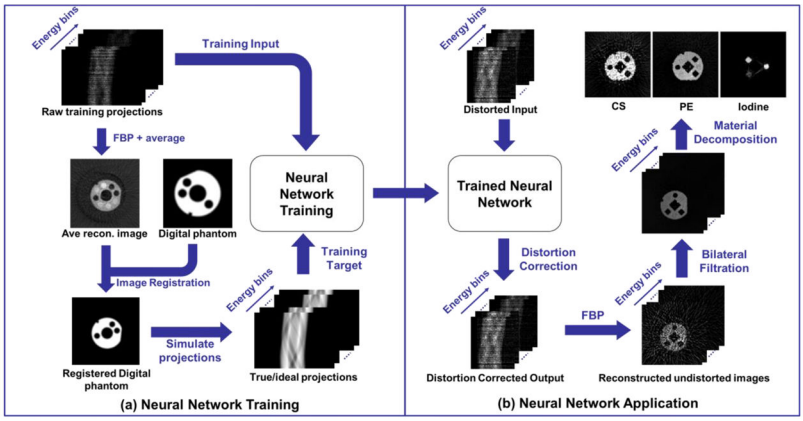

Fig. 2.

A flowchart showing (a) neural network training as a calibration process using a distorted tomographic projection scan of a calibration phantom and its synthesized, digital, ideal projection. (b) Application of the neural network to perform distortion correction before the projections are reconstructed, filtered, and decomposed into basis materials.

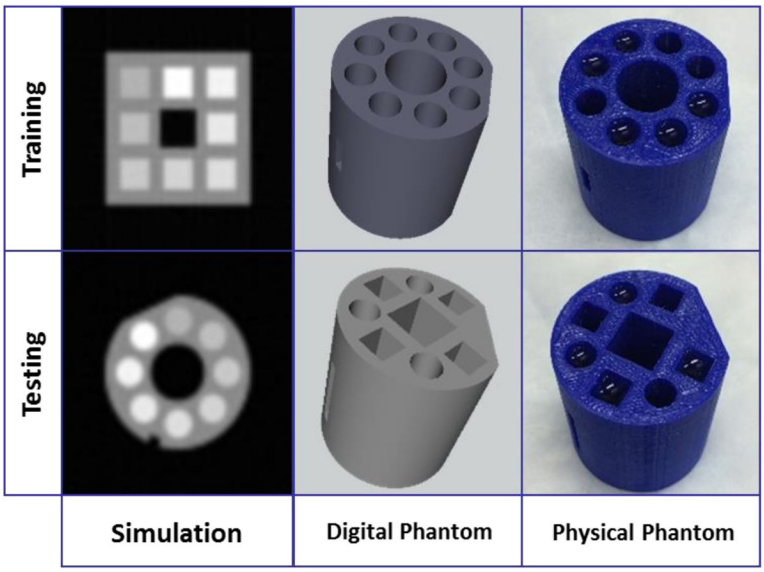

Fig. 3.

Phantoms used in training (first row) and testing (second row) of our neural network. The first column shows phantoms used in simulation containing iodine solution from 0 to 14 mg/ml in water. The second and third columns show the digital models and their corresponding 3D printed physical phantoms used in our experiment for training and applying the neural network, respectively.

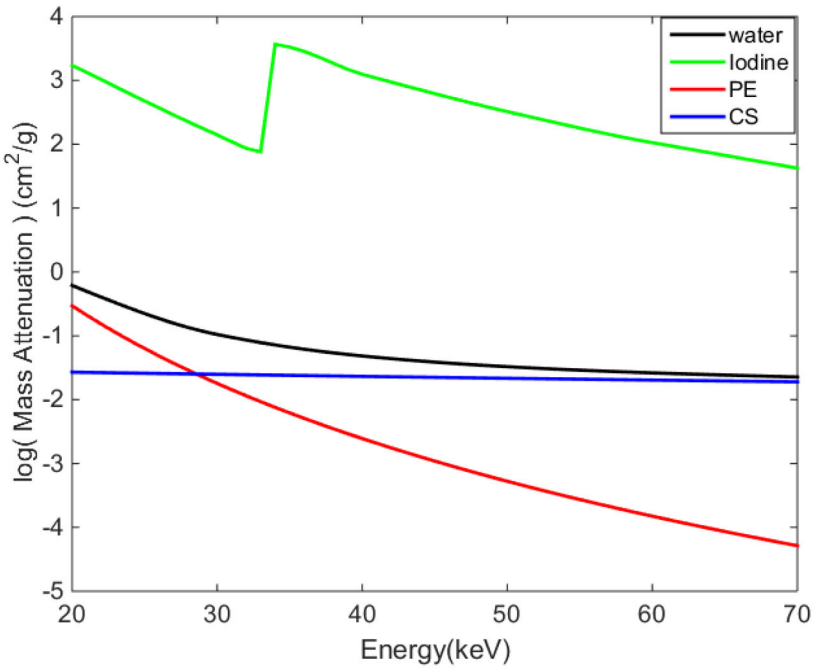

Fig. 4.

Spectral basis functions including the photoelectric effect (PE), Compton scattering (CS), and iodine. The PE and CS functions are scaled to sum to the attenuation of water.

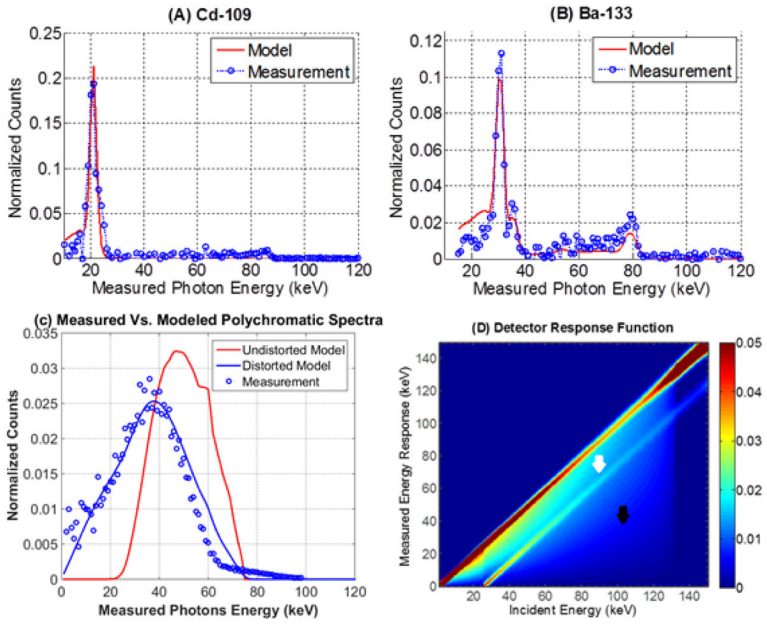

Fig. 5.

Distortion modeling [1]. In (A) and (B) we plot the fitting model and the corresponding measured spectra for Cd-109 and Ba-133, respectively. Plot (C) shows the expected, undistorted 75-kVp polychromatic spectrum (red), as well as the same spectrum after applying the spectral distortion model (solid, blue line). A corresponding measured spectrum acquired with our PCXD at 75 kVp is also shown (blue circles). The 2D display in (D) represents the DRF, showing the low energy tailing effect (black arrow) and the K escape peak for CdTe for incident photons with an energy higher than 25 keV (white arrow).

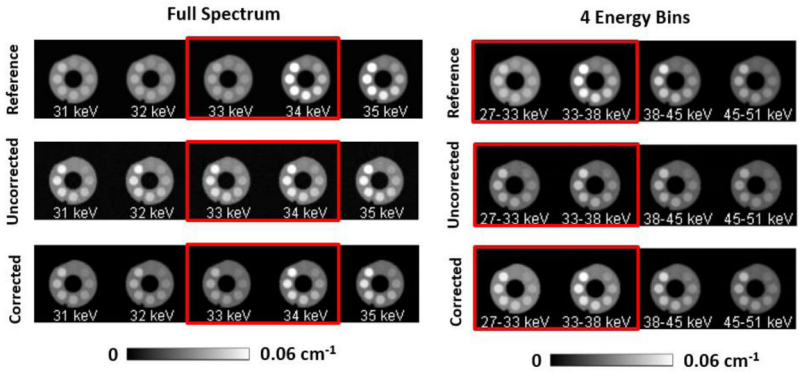

Fig. 6.

Comparison of spectral images for full-spectrum (left) and 4 energy bins (right) before and after applying ANN distortion correction. With correction, the iodine K-edge is clearly visible at 34 keV for full-spectrum mode (red rectangle). The expected results are also shown.

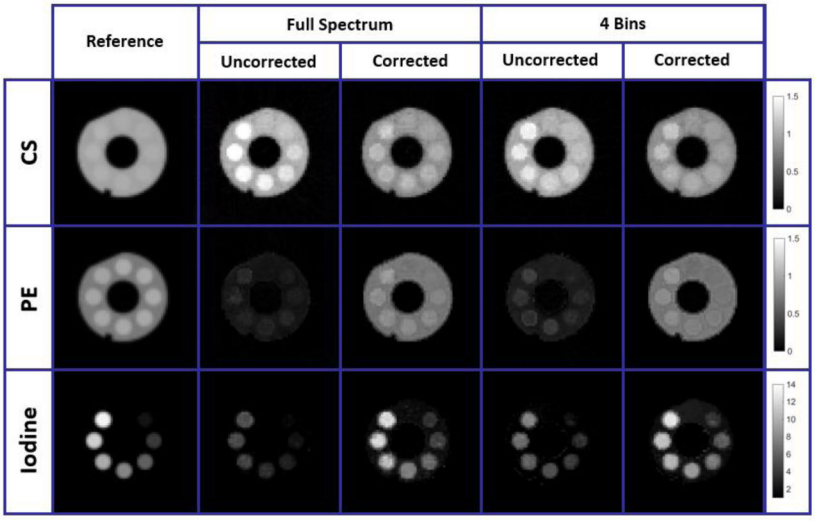

Fig. 7.

The decomposed material images using Compton scattering (CS) and photoelectric (PE) physical basis functions (normalized to water) and iodine from uncorrected and distortion corrected spectral CT data. When uncorrected, the spectral distortion resulted in tremendous iodine contamination in the CS image. Once the distortion was corrected for, the misclassification was reduced, resulting in more uniform images of the vials containing water and the PLA material of the phantom container itself.

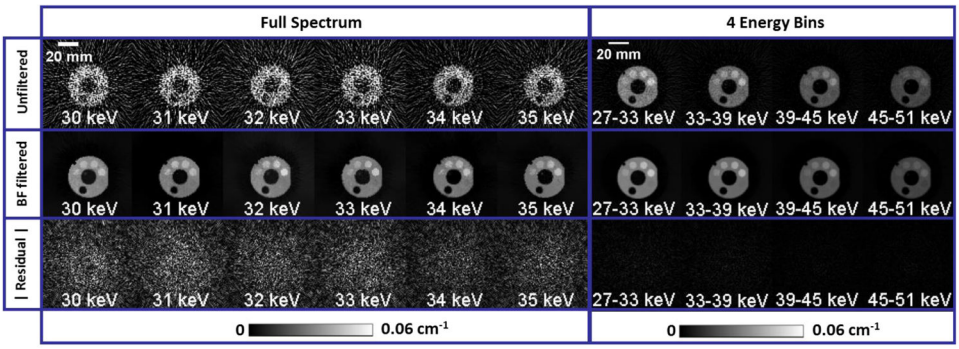

Fig. 8.

Reconstructed images for full-spectrum (left) and 4 bins (right) using FBP from experimental data of the 3D-printed training phantom before and after joint bilateral filtration (BF). The absolute residual images show no visible structure or bias from the filtration operation. For full-spectrum mode, 24 energy bins (from 27 keV to 50 keV) were used to provide the distortion correction.

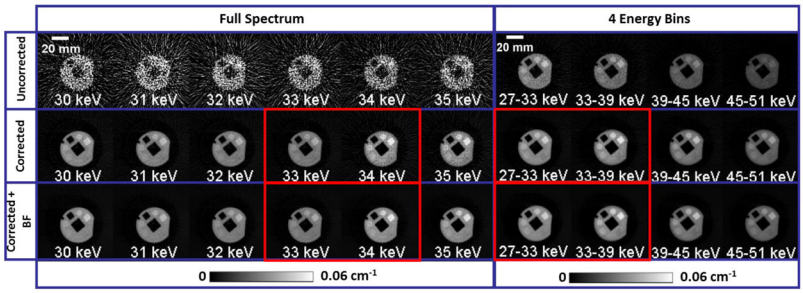

Fig. 9.

Spectral CT images acquired by our PCXD in full-spectrum and 4 bins mode and reconstructed with FBP before and after applying the distortion correction. After the distortion correction, bilateral filtration was applied to further reduce noise. Without correction, the iodine K-edge was smeared out over multiple energy bins. Once distortion was corrected for, the K-edge was notably recovered at ~34 keV (red rectangles).

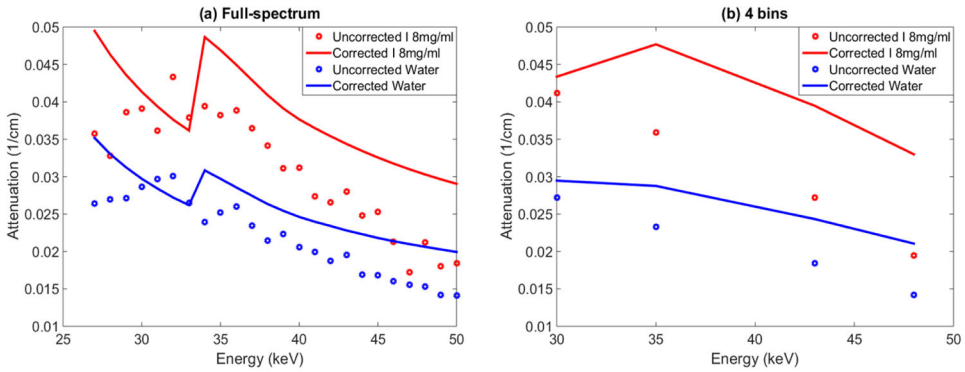

Fig. 10.

Measured attenuation in a vial containing 8 mg/ml of iodine and a vial containing water before (circles) and after (lines) application of ANN distortion correction for **(a)** full-spectrum mode and **(b)** 4 bins mode. The K-edge enhancement from iodine at ~34 keV was notably recovered with the distortion correction. However, there is bias in the water attenuation spectrum at the K-edge of iodine after the correction.

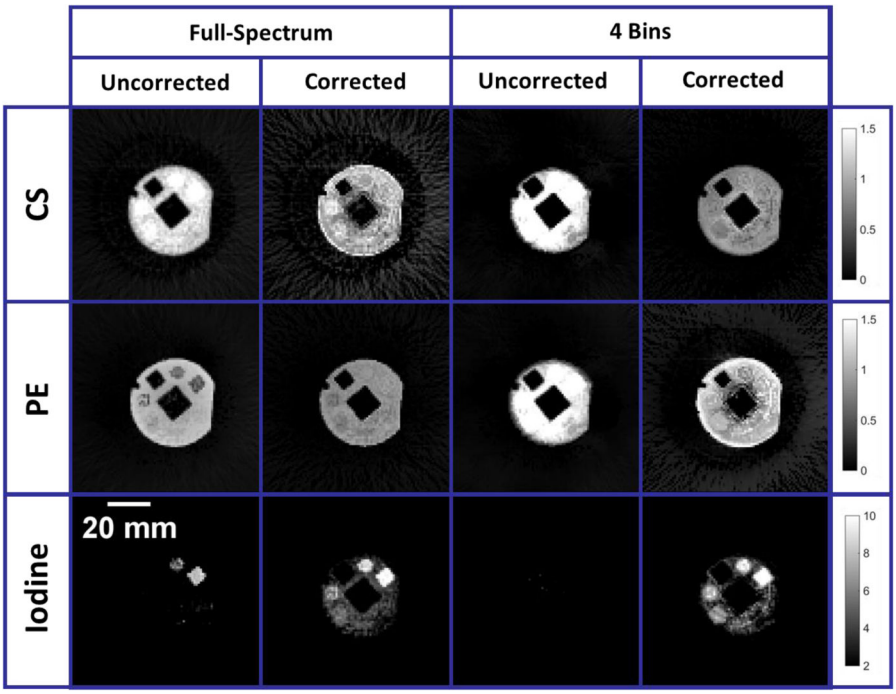

Fig. 11.

Decomposed material images corresponding to full-spectrum and 4 bins mode produced from uncorrected and distortion corrected projections. Without distortion correction, the iodine is greatly underestimated and misclassified into the CS and PE maps. The results are improved with distortion correction.

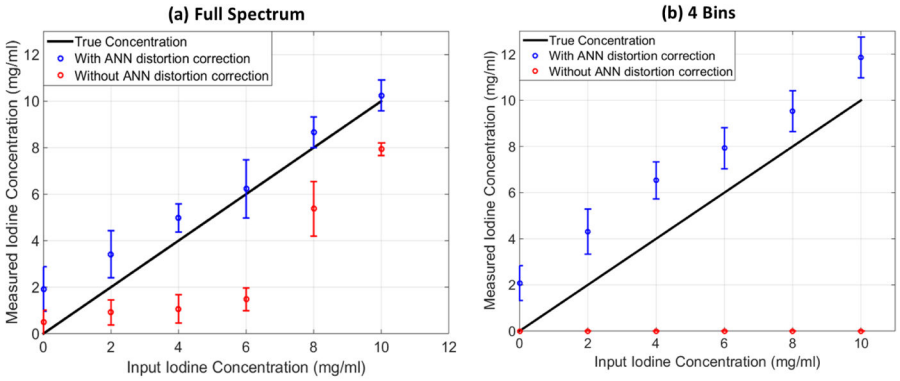

Fig. 12.

Comparison of measured iodine concentrations in (a) full-spectrum and (b) 4 bins mode, with (blue) and without (red) distortion correction. The material decomposition was greatly improved with distortion correction resulting in more accurate iodine concentration estimation.

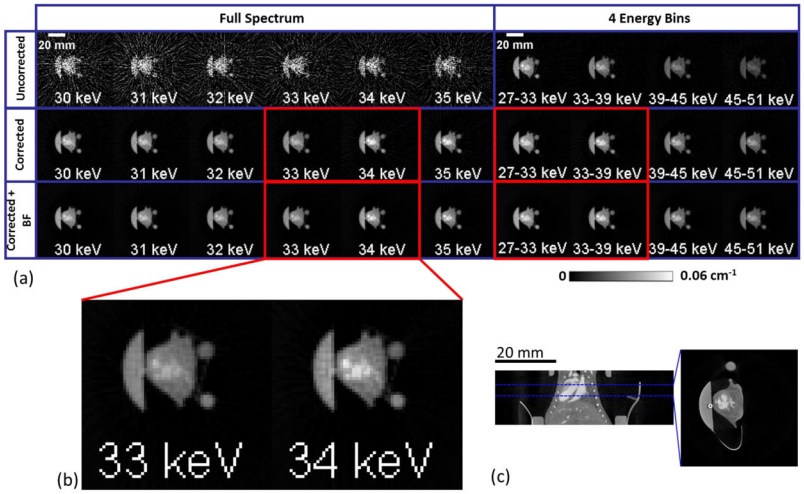

Fig. 13.

(a) Summary of spectral CT results in a mouse scan. 2D cross sectional slices across the heart of the mouse are shown corresponding to energy bins from 30 keV to 35 keV for full-spectrum mode and all bins in 4 bins mode. The images were reconstructed using FBP from distorted projections, distortion corrected projections, and distortion corrected projections with bilateral filtration. The enhancement in the heart corresponds to the presence of iodine in the blood. The loss of K-edge contrast in the spectrally distorted images was recovered by the ANN distortion correction, as highlighted in the jump of enhancement between the 33 and 34 keV energy bins **(b)**. A high-resolution scan is shown in **(c)** to provide an anatomical reference. The reference slice across the heart of the mouse is averaged along the axial dimension to match the resolution of the lower resolution full-spectrum image.

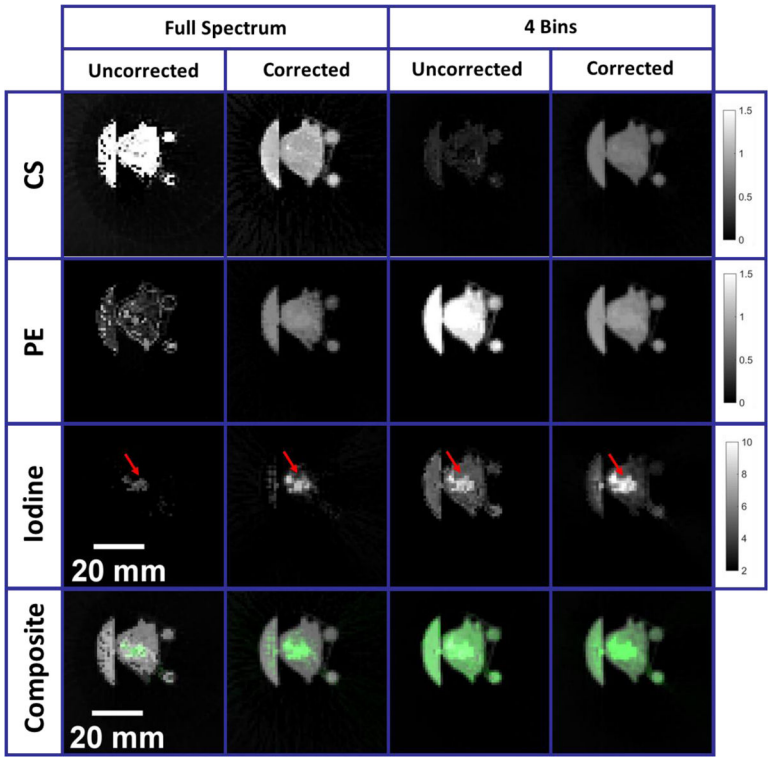

Fig. 14.

Material decomposition of the mouse data for full-spectrum and 4 bins mode. The decomposition was improved with the ANN distortion correction, as shown in the relatively homogeneous CS and PE images. The iodine map appears to be more accurately identified at locations corresponding to the heart (red arrow). The composite images show the iodine map (green) superimposed on the CS and PE images (black and white) without and with distortion correction.

Table 1

Resulting parameter values obtained from [17] and Equations 1 and 2 after fitting the expected and detected spectra for ^{109}Cd and ^{133}Ba.

Parameter	Value
a_1	0.5
a_2	0.015 keV^{-1}
a_3	0.003 keV^{-1}
a_4	0.300×10^{-4} keV^{-2}
a_5	1.16 keV
a_6	0.025

Table 2

Summary of percent relative errors in measured iodine concentration and detectability for full-spectrum and 4 bins mode from our simulation study.

		Measured Percent Relative Error						Mean Error	Detectability (CNR>5)
Iodine Vials		4 mg/ml	6 mg/ml	8 mg/ml	10 mg/ml	12 mg/ml	14 mg/ml		
Full-spectrum	Uncorrected	51%	56%	58%	55%	59%	65%	57%	4–6 mg/ml
	Corrected	7%	8%	7%	3%	0%	14%	7%	<2mg/ml
4 bins	Uncorrected	18%	32%	38%	40%	45%	44%	36%	2–4 mg/ml
	Corrected	42%	24%	11%	3%	10%	9%	16%	2–4 mg/ml

Table 3

Summary of percent relative errors in measured iodine concentration and detectability for full-spectrum and 4 bins mode from our experimental measurement.

		Measured Percent Relative Error				Mean Error	Detectability (CNR>5)
Iodine Vials		4 mg/ml	6 mg/ml	8 mg/ml	10 mg/ml		
Full-spectrum	Uncorrected	73%	75%	33%	21%	**51%**	8–10 mg/ml
	Corrected	24%	4%	8%	2%	**10%**	6–8 mg/ml
4 bins	Uncorrected	-	-	-	-	-	-
	Corrected	63%	32%	19%	19%	**33%**	4–6 mg/ml